Journal of Manufacturing Processes 85 (2023) 90–100

Contents lists available at ScienceDirect

Journal of Manufacturing Processes

journal homepage: www.elsevier.com/locate/manpro

Joining of metal and non-polar polypropylene composite through a simple functional group seeding layer

A.S. Khan [a], F. Liu [a], P. Dong [a,b,*]

[a] Department of Naval Architecture and Marine Engineering, University of Michigan, Ann Arbor, MI 48109, USA
[b] Department of Mechanical Engineering, University of Michigan, Ann Arbor, MI 48109, USA

ARTICLE INFO

Keywords:
Polymer composites
Metal to polymer joining
Friction spot welding
Aluminum alloy
Multi-material
Surface pre-treatment
Bonding interface
Hybrid structures

ABSTRACT

Polypropylene (PP) and its composites are one of the hardest to directly join with metals due to their inherent chemical incompatibility. This paper presents a simple, efficient, and cost-effective method for joining PP composite to aluminum alloy in spot welding configuration by seeding the functional groups via an insert layer of PA6 thin film without requiring surface or material pre-treatment. The resulting joint loading capacity is shown to be sufficiently high to consistently develop failures in PP substrates in lap shear tensile tests away from the bonded area. Joint interface microstructure features are examined in detail. Bonding mechanisms are then described based on the detailed observations obtained in this study.

1. Introduction

Concerns for environmental sustainability and demands for vehicle performance continue to drive major vehicle manufacturers to pursue more advanced lightweight structure solutions [1,2]. Most recent studies have shown that multi-material structures are the most effective way of achieving structural lightweighting in transportation vehicular systems by "using the right material at the right place" [3,4]. Cost-effective manufacture of reliable multi-material structures, e.g., made of lightweight metals and polymer composites, has been considered one of the major challenges for realizing the benefits of these advanced lightweight vehicular structures [3,5]. These multi-material structural design scenarios often require combining steels, and aluminum alloys with various polymeric composites through either direct or indirect welding and joining methods.

One of the key challenges in manufacturing multi-material structures in a mass-production environment is how to cost-effectively achieve strong bonding between metal and polymer composite. Traditionally, metals and polymers were typically joined together using adhesives and/or mechanical fastening methods. Adhesive joining requires significant curing time under the support of special fixtures, and its byproducts sometimes can be hazardous to the environment [7]. Mechanical fastening using rivets, nuts, bolts, and mechanical engraving, adds additional weight to the hybrid structure, creates stress concentration sites that are prone to fatigue failures, and cannot attain hermetic sealing [8,9]. These issues can be addressed to a large degree by developing robust welding methods capable of joining metal and polymer composites directly [10–12]. In the past decade, some advanced welding concepts were investigated for joining metals and polymer/polymer composites, such as friction lap welding (FLW) [13–17], ultrasonic welding [18,19], laser direct welding [20–23], induction welding [24], and resistance spot welding [25]. Among these newly developed welding methods, FLW has the advantages of high welding speed, good bonding strength, fewer process parameters to control, low material and mechanical property losses, and the absence of environmental hazards [13,14]. It should be noted that some of these welding methods mentioned above have been demonstrated to be able to produce considerable high bonding strength between metal and polyamide (PA) based materials without special preprocessing or surface modifications [13,26,27]. However, to our best knowledge, none of them can be used successfully for joining metal and polypropylene (PP) based composite materials which are widely used in auto-body closures [16,28].

The major difficulty can be attributed to the PP polymer's molecular structure [27]. It has been shown that various metals can be welded directly to polymethylmethacrylate (PMMA) [29], polycarbonate (PC) [30], polyethylene terephthalate (PET) [20,31], PA [13,18,25,32–35], polyether ether ketone (PEEK) [24,36–39], and polyetherimide (PEI)

* Corresponding author at: Department of Naval Architecture and Marine Engineering, University of Michigan, Ann Arbor, MI 48109, USA.
E-mail address: dongp@umich.edu (P. Dong).

https://doi.org/10.1016/j.jmapro.2022.11.022
Received 4 August 2022; Received in revised form 20 October 2022; Accepted 9 November 2022
Available online 22 November 2022

[19]. All these polymers contain carbonyl functional groups (C═O). Liu et al. [27] demonstrated that the carbonyl group on the thermoplastic surface reacted with aluminum atoms on the surface of aluminum alloys once an intimate contact can be created during the welding, leading to the formation of strong C—O—Al chemical bonds at the bonding interface. Liu et al. [27] also concluded that it is difficult to directly weld metals to thermoplastics that do not contain polar functional groups, such as polypropylene, and polyethylene without any surface or material modifications.

To overcome the difficulties associated with the lack of polar functional groups, special surface modifications of metal and/or PP sides, therefore, have been explored for increasing their weldability. Additional physical and chemical treatments have also been examined to introduce geometrical features at a microscopic scale on the metal surface to promote micro-mechanical interlocking between metals and PP under different welding conditions [28,40]. Along this line, the application of a silane coupling agent on the metal surface has been proven beneficial for enabling the bonding between the metal and PP [25]. Surface modification of PP by plasma treatment [41] and bulk polymer modification by maleic anhydride grafting [42,40] have also been useful for joining PP with metals. These promising outcomes were attributed to the contributions of plasma treatment which generated transient functional groups on the PP surface and maleic anhydride grafting that contains carbonyl functional groups [44,45]. On the other hand, micro-mechanical anchoring provided by laser texturing has also become a suitable means to provide the joining through a mechanical interlocking mechanism when the functional groups are absent in the polymer [28] or when to fulfill the requirement of joint strength improvement [36].

PP has the lowest polymer density and its composites have been very cost-effective among other available thermoplastic composites [46–48]. Demands for PP-based composites for producing metal-polymer hybrid structures have been surging in recent years in the automotive industry due to the significant advancements in thermoplastic composite manufacturing [49,50]. Even though the surface modification methods mentioned above have shown their efficiency in enhancing the bonding strength between metals and PP, these methods are still less attractive for the mass-production industry for which low manufacturing cost and production throughput are the main drivers.

To address some of the challenges mentioned above, this study is focused on the development of a robust and direct PP to metal joining method. Specifically, here we consider the combination of 6061 aluminum alloy (AA6061) and PP-based glass fiber reinforced polymer composite (GFRP-PP) through a spot weld configuration. Through a simple and inexpensive carbonyl group seeding technique, it can be shown that strong chemical bonding at the GFRP-PP and AA6061 interface can be consistently established, resulting in strong bonding strengths. Both mechanical and interfacial microstructure characterizations are then performed for characterizing the resulting bonding interface quality and effects of various process parameters. The underpinning bond formation mechanisms at the joint interface between AA6061 and PP-based GFRP-PP are also discussed.

2. Materials and methods

AA6061 and GFRP-PP containing 40 % glass fibers were used in this study. The physical and mechanical properties of both materials are listed in Table 1. As a point of reference, the conventional friction-assisted joining process is demonstrated in Fig. 2(a) and a non-consumable heat-treated flat head steel tool of 20 mm diameter used is shown in Fig. 2(b). Corresponding forge force and forge depth variations as a function of weld time are shown in Fig. 2(c). A modified version of the friction-assisted spot joining schematic is shown in Fig. 3 (a), in which an off-the-shelf 50-μm thin PA6 film was placed for seeding the functional group as an inter-layer between AA6061 and GFRP-PP (Fig. 3b and c). Note that the color of the PA6 film is chosen only for providing a sufficient contrast in subsequent bonding surface examination. The physical and thermal properties of the PA6 film are listed in Table 1 and the chemical composition of AA6061-T6 is listed in Table 2. The dimensions of the specimen used are shown in Fig. 4(b–c). The aluminum sheet was polished with P400 sandpaper and then degreased with ethanol before joining. No special surface or bulk material modification was performed on the GFRP-PP composite.

Table 1
Mechanical and physical properties of AA6061-T6, 40GFRP-PP, and PA6.

	AA6061-T6	40GFRP-PP	PA6
Ultimate tensile strength (MPa)	310	115	85
Yield strength (MPa)	242	–	–
Elastic modulus (GPa)	68.9	8.66	3.30
Elongation at break (%)	12.50	4.50	40
Melting temperature (°C)	476–660	165	230
Thermal conductivity (W m^{-1} K^{-1})	167	0.30	0.25
Coefficient of thermal expansion (μm m^{-1} K^{-1})	23.6	45	90

Sandwich assembly using PA6 inter-layer was prepared as shown in Fig. 3(a–b) and an initial force of 150 N using the said flat head tool was applied to maintain close contact between metal and composite sheets. Friction-assisted spot joining was then performed at a constant tool rotation rate of 1800 rpm under displacement control mode. Forge depth was varied from 0.05 to 0.15 mm and spot weld times of 3, 6, and 12 s were used.

Three K-type thermocouples were used to measure the interface temperatures and their embedded arrangements are shown in Fig. 9 (a–b). Lap shear tensile experiments were performed to obtain the joint strength in an MTS load frame at a displacement rate of 1 mm/min (Fig. 4a). Cross-sectional analyses at macro and microscopic levels were performed along the section BB′ (Fig. 9a) using Nikon DIC optical microscope (OM) and a JEOL IT500 scanning electron microscope (SEM). SEM observations were carried out at 5 kV–15 kV accelerating voltage under secondary electron detector (SED) mode and at 15 kV accelerating voltage under back electron detector (BED) mode. The lengths of the bonding regions were measured along the aluminum surface at the cross-sections and the depths of the melting region were measured under the nugget center (Fig. 6a–b).

3. Results

As stated in the previous section, due to its non-polar nature (Fig. 1a), low surface energy, and hydrophobicity, PP-based composite does not join with any metal without any special surface or material pre-treatment. After the initial polishing and degreasing, several welding trials were conducted to join AA6061 and GFRP-PP using the reference welding parameter variation as shown in Fig. 2(c), and the resulting scenarios are presented in Table 3. As can be seen in Table 3, none of the welding parameter combinations could produce the joining between AA6061 and GFRP-PP, and sheets of both materials fell apart (Fig. 2d) as soon as the tool was lifted from the metal surface. Consequently, no significant polymer residue was observed on the metal side (Fig. 2d).

3.1. Bonding enabled by carbonyl group seeding

Fig. 3(d–f) illustrate a strongly bonded joint between AA6061 and GFRP-PP composite substrates, in contrast to Fig. 2(d) which shows no signs of bonding at all. The inter-layer of PA6 thin film enabled the formation of a strong bond between these two materials without requiring any special surface or material modifications either on the metal or GFRP-PP side. Fig. 3(d–f) represent a specimen produced at 1800 rpm, 12-s spot weld time, and 0.10 mm forge depth before and after the lap shear tensile experiment. Except for the plastically deformed region under the tool impression, no noticeable thermo-mechanical distortion was seen on either side of the specimens

Table 2
Elemental composition of AA6061-T6 sheet (wt%).

	Al	Si	Zn	Fe	Cu	Mg	Ni	Mn	Ag	Cr	Others
AA6061	Balance	0.17	0.11	0.11	0.10	0.08	0.03	0.03	0.01	0.05	<0.025

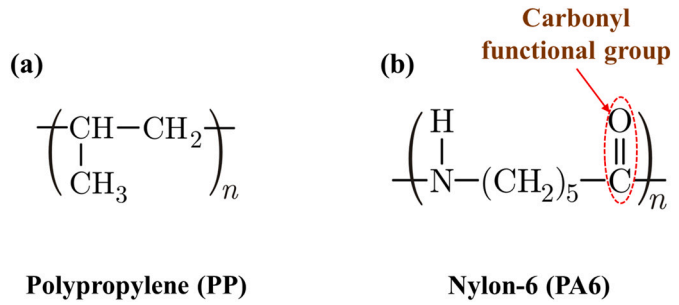

Fig. 1. Chemical structure of (a) polypropylene (PP) without any functional group, (b) nylon-6 (PA6) containing carbonyl functional group.

(Fig. 3d–f). Fig. 3(f) shows the base material failure, suggesting a much stronger joint than the base GFRP-PP composite material.

The failure location is at some distance away from the tool center, indicating a sufficiently developed interfacial bonding between both materials, which offers sufficient joint strength. It should be emphasized here that the joining method demonstrated here requires no special bulk or surface modifications on either material side, unlike the existing methods either using surface treatments [28] or bulk material modification methods [42,44,51]. It should be pointed out that maximum loads at failure not the joint strengths are compared to determine the maximum load capacity of the joints. For deriving joint strength in terms of stress at failure for comparing with other specimen types (e.g., cross-tension [52,53]) or structural applications, the mesh-insensitive structural stress methods [54–56] can be used, which is beyond the scope of this study.

3.2. Joint strengths, failure modes, and key welding parameters

Joint strengths were evaluated using lap-shear specimen design configuration (see Fig. 4a through c) typical of those used for spot welded specimens [28,37] under different welding conditions in terms of friction tool forge depth and welding time. The results are shown in Fig. 4(d) corresponding to a constant tool rotation rate of 1800 rpm. Two important observations can be made from the lap shear tensile test results obtained in Fig. 4(d). First, the spot weld time has significant effects on the joint load capacity (measured as the load at failure). The load at failure increases with spot weld time and reaches its maximum value when the weld time reaches about 12 s, when tensile failure within the PP substrate at some distance away from the spot weld area occurs, hereafter referred to as base material failure mode. The apparent lower failure loads with weld time of less than about 12 s can be related to insufficient bond formation at the interface, leading to the interfacial failure mode, i.e., failure along the interface between the aluminum and PP substrates, as shown in Fig. 5(a) through (f). Second, welding forge depth within the range considered did not influence the joint load capacity in any significant manner. As can be observed from Fig. 4(d), all three forge-depths resulted in similar levels of loads at failure in all cases. Also, as stated in Section 2, an initial contact force of around 150 N was used to keep both material sheets in close contact to avoid any gap between the joining surfaces before starting the process. This suggests that the forge depth does not affect the joint formation significantly as long as an initial minimum contact force is maintained between both the

Table 3
Summary of welding trials to join AA6061 and GFRP-PP without PA6 thin film inter-layer and any special surface or material pre-treatment.

Spot weld time (s)	900 rpm 0.10 mm	1800 rpm 0.10 mm	1800 rpm 0.15 mm
3	No joining	No joining	No joining
6	No joining	No joining	No joining
12	No joining	No joining	No joining
25	No joining	No joining	No joining

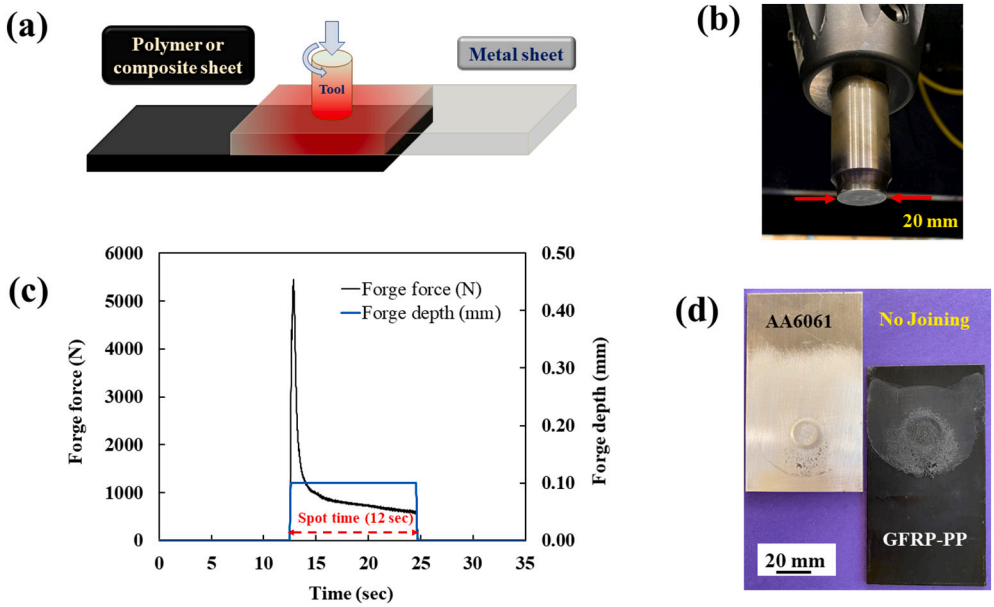

Fig. 2. (a) Schematic of a friction spot joining method, (b) non-consumable steel tool, (c) forge force and depth variation during the main phase of friction assisted joining process, (d) non-joinable AA6061 and GFRP-PP by conventional method.

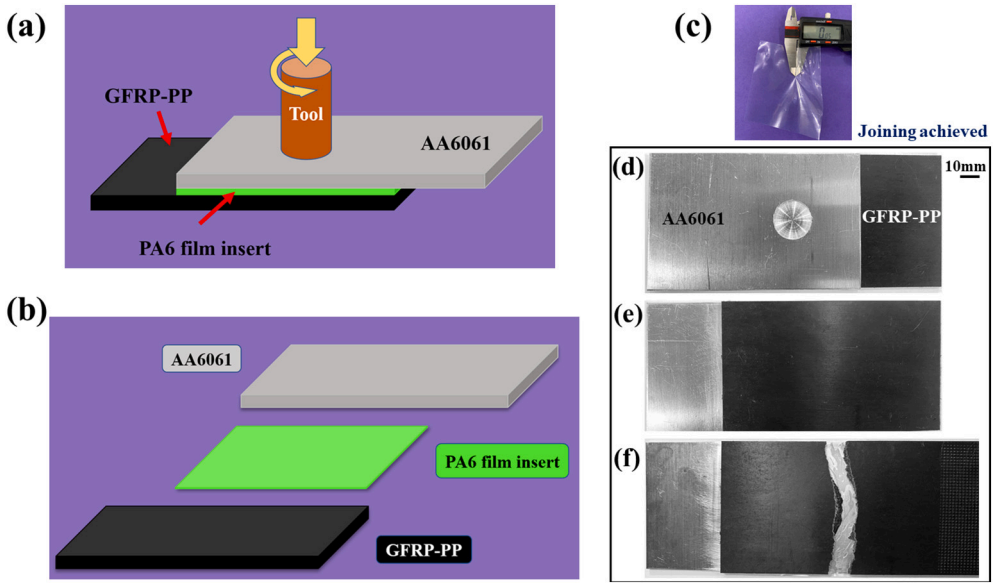

Fig. 3. (a) Schematic of friction spot joining method using thin film insert, (b) detailed view of material placement during joining, (c) 50 μm thin PA6 insert film, (d) top view of the AA6061/GFRP-PP joint produced using thin PA6 film [1800 rpm, 12 s and, 0.10 mm] before the lap shear tensile test, (e) bottom view of the joint produced before the lap shear tensile test and, (f) bottom view and base material failure of the joint produced after the lap shear tensile test.

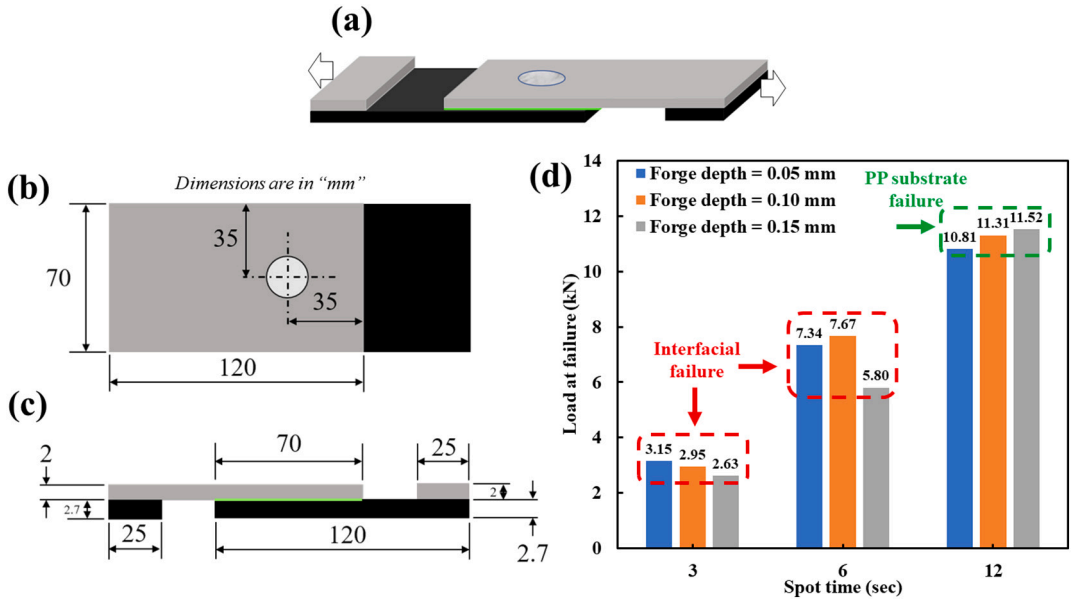

Fig. 4. (a) Lap shear tensile test schematic, (b) & (c) major dimensions of the specimen used, (d) summary of the peak loads at failure during lap shear tensile test.

materials.

As substantiated in Fig. 5(a) through (f), within the cases exhibiting interface failure mode corresponding to weld time being <12 s, the increase in failure loads shown in Fig. 4(d) can be attributed to the increase in interfacial bonding area indicated by the overall increased area size of PP composite residues sticking to the aluminum substrates. As the weld time reaches about 12 s, the failure mode transitions to base material failure in PP composite substrates (Fig. 5g through i) in all cases resulting in the maximum joint load capacity given in Fig. 4(d).

3.3. Interfacial microstructure characterization

SEM micrographs of the cross-section in Fig. 6(a–b) further elucidate the bonding interface and bond-line microstructure features of the joint developed between AA6061 and GFRP-PP at 1800 rpm, 12 s spot weld time and 0.10 mm forge depth. A mixed network of polymers and randomly distributed glass fibers across the composite side can be seen in Fig. 6(a) without any fiber penetration through or across the aluminum surface. Since the peak process temperature is above 350 °C (Fig. 9c), both polymers must generate various chemical compounds through pyrolysis at elevated temperatures. Consequently, gases and bubbles form in the viscous polymer melt and migrate away from the aluminum surface under high pressure. These bubbles become cavities during polymer re-solidification and are encircled in Fig. 6(a).

An intimately bonded interface between AA6061 and PA6 near the aluminum surface and a significant amount of PA6 dispersion toward the GFRP-PP composite side can be further observed in Fig. 6(b). A network of PP matrix, glass fibers, and PA6 wrapping the glass fibers in the re-solidified polymer melt are highly pronounced below the aluminum surface (Fig. 6b). It suggests that frictional heat melted the

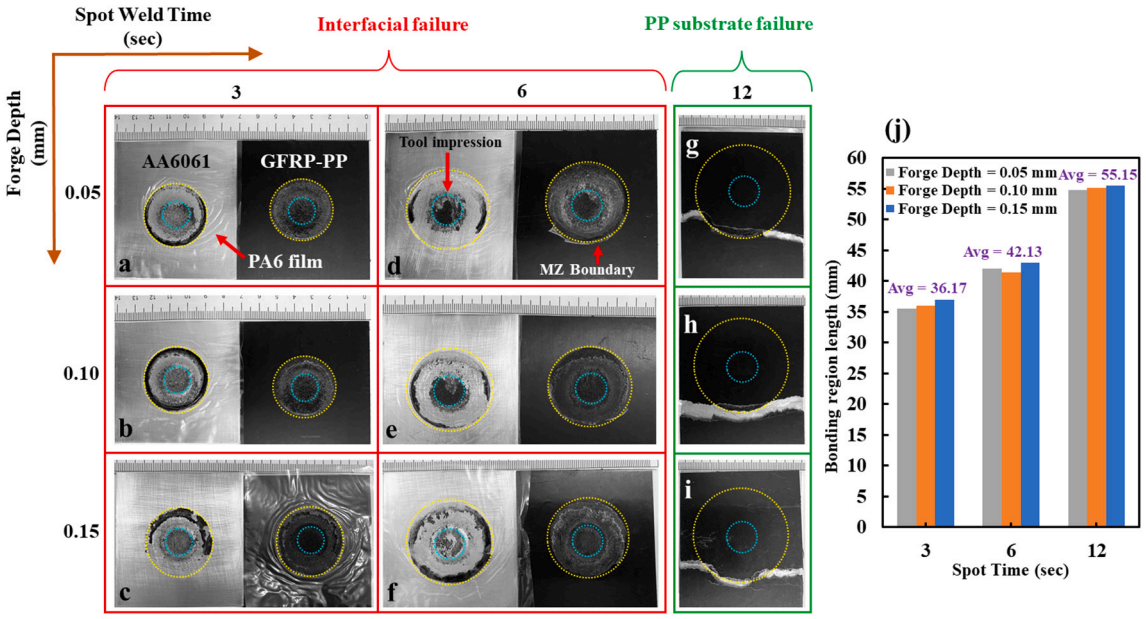

Fig. 5. (a–i) Failure patterns after lap shear tensile test of AA6061/GFRP-PP joints produced using PA6 thin film inter-layer [1800 rpm, various forge depth and spot weld time], (j) comparison of the bonding region lengths measured as the outer diameters of the melting zone (MZ).

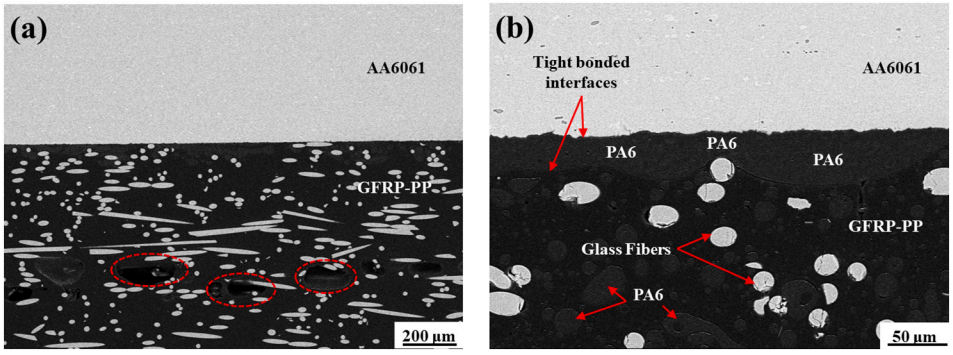

Fig. 6. Cross-sectional SEM images of AA6061/GFRP-PP joint [1800 rpm, 12 s and 0.10 mm], (a) low magnification SEM micrograph with visible cavities, (b) high magnification SEM micrograph depicting bonding interface and PA6-fibers-PP network.

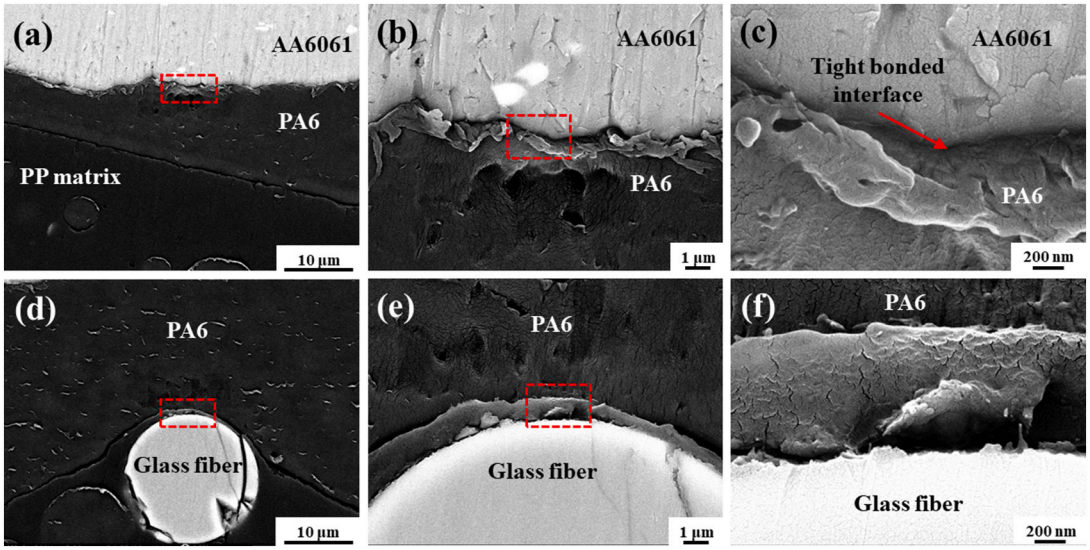

Fig. 7. SEM images of bonding interfaces in AA6061/GFRP-PP joint [1800 rpm, 0.10 mm and 12 s], (a–c) Al-PA6 interface, (d–f) PA6-fiber interface.

PA6 and PP matrix, and glass fibers were physically inter-mixed again between these polymers. The system then re-solidified as a multi-material composite network near the aluminum surface.

Fig. 7(a–c) show a tightly bonded AA6061 and PA6 interface. The boundaries are non-distinguishable at the nanoscale and can be seen intimately fused (Fig. 7c). Fused boundaries suggest intimate bonding between both materials without any significant mechanical interlocking features. The intimate bonding between the AA6061 and PA6 consistently prevails for most of the joint bond-line (Fig. 6a–b), although the spread of PA6 varies with respect to the nugget center location (Figs. 6b and 12).

Fig. 7(d) shows a glass fiber surrounded by the PA6 and another 400 nm thick layer of unidentifiable material which is further observed in Fig. 7(e–f) between PA6 and the glass fiber. Since PP was reinforced by 40 % glass fibers in GFRP-PP, the residual layer may be a layer of PP matrix that remained on the fiber during the melting and re-solidification of polymers. It suggests that despite a thin layer of residual material on the glass fiber, PA6 is surrounding the glass fibers intimately, and formulates a strong multi-material composite network with GFRP-PP. A further molecular level adhesion characterization of this interface is beyond the scope of this article.

Fig. 8(a–c) illustrate a noteworthy feature between PA6 and PP matrix materials. In general, PA6 and PP polymers are incompatible to mix and do not interact chemically due to their significantly opposite polar characteristics [43,57]. PA6 is polar in nature (Fig. 1a) due to the presence of oxygen and nitrogen as electronegative species, whereas PP does not have any such electronegative species in its chemical structure (Fig. 1b), making these two polymers chemically incompatible with each other [57]. However, we can observe an undefined interaction between both polymers at the nano-scale level and three-dimensional fibrillar linkages of PA6 can be seen diffusing in the PP matrix (Fig. 8b–c). Probable molecular chain entanglement either at a physical level or chemical mixing of both the polymers under high temperature and pressure conditions can be attributed to this phenomenon and, a comprehensive physical and chemical analysis is necessary to provide more meaningful insights further in the future.

Interfacial temperature histories are examined, as shown in Fig. 9. Fig. 9(a–b) show the embedded thermocouple placements during spot welding corresponding to 1800 rpm friction tool rotation, 12-s spot weld time, and 0.10 mm forge depth. Fig. 9(c) shows the interfacial temperature history measurement data corresponding to the three interfacial positions described in Fig. 9(b). As can be seen in Fig. 9(b), thermocouple-1 (TC1) was placed at the centerline of the nugget, TC2 was placed underneath and adjacent to the tool boundary (tool diameter 20 mm) and, TC3 was placed where the through-thickness failure initiation of GFRP-PP was observed (just before 23.50 mm from the nugget center). TC1 provided the temperature profile under the nugget center and reached a maximum of 394 °C representing the overall peak process temperature (Fig. 9c). This indicates a high frictional heat diffusion radially inwards increasing the temperature at the center higher than in other locations. TC2 and TC3 registered maximum temperatures of 336 °C and 185 °C respectively (Fig. 9c). Also, TC1 maintained a comparatively higher temperature than TC2 and TC3 throughout the process. This can be attributed to the farther positions of TC2 and TC3 from the nugget center and unavoidable losses of frictional heat while diffusing radially outwards from the center.

As can be seen in Fig. 9(c) that all the thermocouples maintain temperatures higher than 165 °C after a 6-s spot weld time where 165 °C represents the melting point of the PP matrix. The thermal decomposition of pristine PP and PA6 starts above 355 °C and 398 °C respectively and glass fiber reinforcement can increase the decomposition temperature for GFRP-PP further beyond 425 °C [58,59]. Additionally, as shown in Fig. 9(c), the peak process temperature measured (TC1 peak) is near 400 °C, and the TC1 temperature profile is above 350 °C for most of the joining process duration. This indicates a reasonable possibility of partial thermal decomposition of both the polymers near the tool center. However, TC2 and TC3 temperature profiles are well below the decomposition temperatures, suggesting no significant thermal decomposition of both the polymers away from the tool center. Corresponding melting zone (MZ) diameter from Fig. 5(j) and decomposition zone (DZ) diameters are further used to obtain MZ/DZ and are shown in Fig. 9(d). It can be observed that the 12-s spot welding significantly increases the MZ/DZ corresponding to the stabilized temperature regime in Fig. 9(c) beyond 6-s spot weld time.

3.4. Fracture surface analysis

Posterior analyses of fracture feature further elucidate the bonding phenomenon between AA6061 and GFRP-PP due to the thin PA6 insert layer and are shown in Fig. 10(a–d). Joints developed at 1800 rpm and 0.10 mm forge depth were selected owing to the reasons stated in earlier sections. Fig. 10(a) and (b) show the interfacial fracture features of 3-s and 6-s spot-welded joints respectively. Due to their different failure surface morphologies, three distinct bonding regions can be observed. Region-1 (R1) contains the area with a noticeable tool impression under the aluminum sheet and receives the highest amount of heat during the joining process to attain the peak process temperature (Fig. 10b). Region-2 (R2) is the shiny area beyond R1 with a significant amount of PA6 residue on both aluminum and PP composite sides (Fig. 10b). Region-3 (R3) is the outermost thick ring of re-solidified PP and PA6 residues surrounding R2 (Fig. 10b). All the regions are shown in Fig. 10 (b) and can be seen evolving with spot weld time conforming with Fig. 5. Other researchers [13,28,60] have used different terminologies for such regions responsible for bonding based on similar thermomechanical and adhesion characteristics.

Furthermore, Fig. 10(a) shows a spread of PP residue (blackened area) and fibers in R1 starting at a 3-s spot weld time. PP residue and fibers' density increase for the 6-s spot weld time in R1 on the aluminum side as shown in Fig. 10(b) and are expected to increase further for the 12-s spot weld time. Due to high heat input, a large amount of polymer must melt in R1 and flow outside the R1 under high tool pressure, leaving a shiny saddle transition surface surrounding R1 (Fig. 10b). Similarly, due to high heat, the density of gaseous bubbles must be high in R1 compared to surrounding areas. Consequently, R1 shows interface failure features, and the fracture surfaces on the aluminum side depict the morphology of intermittently broken bubbles, cavities, and polymer

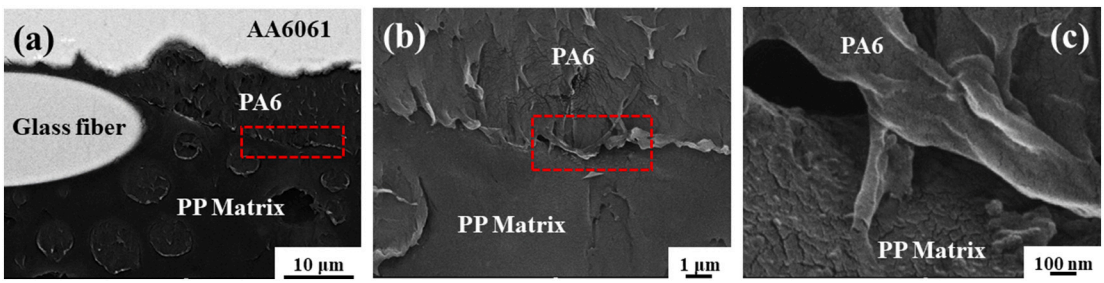

Fig. 8. SEM images showing possible PA6-PP interface in AA6061/GFRP-PP joint [1800 rpm, 12 s and 0.10 mm].

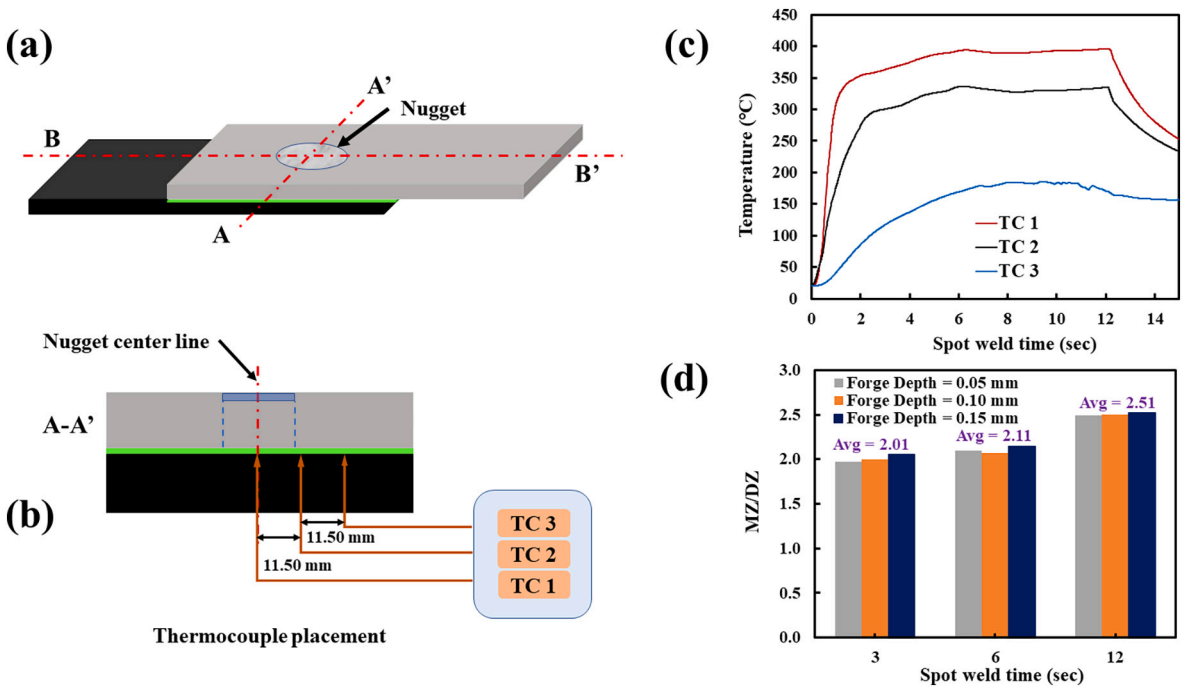

Fig. 9. Interfacial temperature measurement, (a–b) schematic of thermocouple (TC) placement, (c) temperature measurements for AA6061/GFRP-PP joint [1800 rpm, 12 s, 0.10 mm] and, (d) ratios of MZ to DZ for various process parameters.

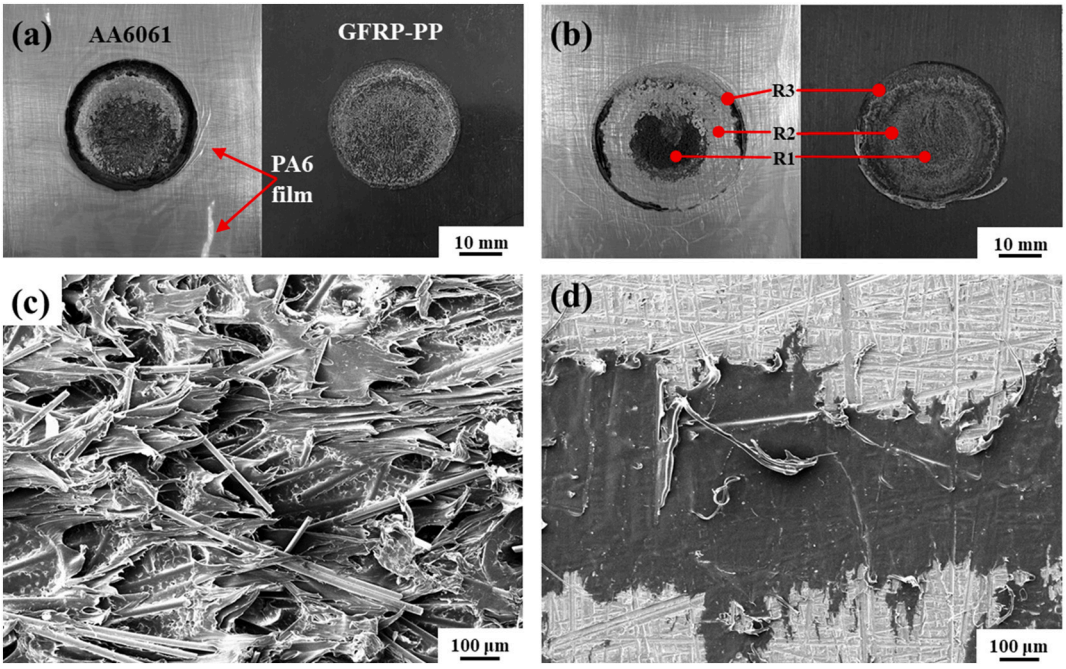

Fig. 10. Failure features of the produced joints [1800 rpm, 0.10 mm] at, (a) 3-s spot weld time, (b) 6-s spot weld time, (c) SEM micrograph of R1 on aluminum side, (d) SEM micrograph of R2 on aluminum side.

network tearing (Fig. 10c). Dominated by high bubble and cavity concentrations and resultant failure features, R1 alone cannot provide high joint strength.

On the other hand, R2 has a different correlation with spot weld time compared to R1. As can be seen in Figs. 5 and 10(a–b), the width of R2 increased significantly both in aluminum and PP composite sides with spot weld time. R2 has an opaque residue of PA6 material which increases both on aluminum and PP composite sides with increasing spot weld time. The PA6 residue in R2 is not consistently uniform and spots of shiny aluminum surface also appear in R2 on the aluminum side (Fig. 10d). Its mixed spread on both aluminum and GFRP-PP sides suggests that R2 has both adhesive and cohesive failure features as can be seen in Fig. 10(b & d). Furthermore, R2 has only minute traces of glass fibers as can be seen in Fig. 10(d). The absence of fibers in R2 at the aluminum side, suggests that PA6 film melted and resolidified with glass fibers of GFRP-PP to form a strong multi-material composite network in R2. The fiber network between PA6 and glass fibers is significantly stronger than the PA6 and aluminum bonding in R2 and does not break

in PP composite (Fig. 10d). The absence of any cavity-breaking features in R2 implies that bubbles if formed, should be very few in R2. A further increase in spot weld time from 6 s must melt and resolidify a higher amount of PA6 and PP matrix in R2 and further increase the bonding strength. Owing to the low possibility of bubbles and a combination of adhesive-cohesive failure features, R2 should provide a high contribution toward overall joint strength. This fact is more pronounced in the 12-s spot-welded joint (Fig. 11) which failed in the base PP composite material.

The outermost region R3 has a different morphology compared to R1 and R2 as shown in Fig. 10(b). The outer diameter of R3 increases significantly with spot weld time as can be seen in Fig. 10(a) and (b). It has a thick blackened ring of re-solidified material when spot weld time is 3 s (Fig. 10a), and it partially diffuses with PA6 when spot weld time increases to 6 s (Fig. 10b). The outer edge of R3 for the 12-s spot-welded specimen suggests that it has ridge patterns (Fig. 11b–d). Ridges form due to the squeezing action of molten viscous polymers away from the nugget center during the joining process. These ridges further formulate bulk material waviness in R3 when re-solidified, causing material discontinuities. Such melt flow and re-solidification caused material discontinuities in R3 must increase the stress concentration significantly near the outer edge of R3 (Fig. 11b–d). Consequently, the fracture location appears near the edge of R3 as shown in Fig. 11(b). It further follows from the morphologies and failure features that; qualitatively, bonding regions should follow a ranking of R2 > R1 > R3 toward the joint strength contribution. In other words, the boundary of the R1 corresponds to the DZ and the boundary of the R3 corresponds to the MZ. As shown in Figs. 5 and 9(d), the fracture mode transitions from the interfacial failure mode for the 3 and 6-s spot weld time, to BM failure for the 12-s spot weld time when the MZ/DZ increases to the maximum attainable value.

4. Discussions

4.1. Bonding mechanisms

It is worth noting that all AA6061 aluminum substrates used in this study were subjected to polishing using P400 sandpaper and degreasing with alcohol. The polishing process with P400 sandpaper typically provides surface roughness of around 30 μm without any significant depth and is not sufficient to achieve a strong micro-mechanical interlocking effect [28]. AA6061 and GFRP-PP did not join without the PA6 inter-layer (Fig. 2d and Table 3) after AA6061 surface polishing and degreasing using P400 sandpaper. However, using the same surface degreasing process, strong joining between AA6061 and GFRP-PP (Figs. 3d–f and 5) was achieved when using the PA6 inter-layer, and, joining can be solely attributed to the application of functional group seeding inter-layer via PA6 thin film. The temperature profile due to the frictional heating in Fig. 9(c) suggested that all the joining regions were either at the melting temperature of the PP matrix or higher and TC1 and TC2 remained above the melting temperature of PA6 throughout the joining process suggesting sufficient melting of both PA6 and PP matrix and mixing with the glass fibers to formulate the multi-material composite network. This multi-material composite network initiated at the AA6061 surface with the PA6 formulated an intimate interface with the AA6061.

Due to the presence of functional groups, PA6 must react strongly with metals and should be the major contributor to the strongly bonded interface between aluminum alloy and PA6 [14,27]. Liu et al. [27] proved that the formation of the C-O-Al type of chemical bond is a highly probable cause for providing intimate bonding between aluminum and PA6 type polymers. In addition, other researchers have suggested other possibilities of different chemical interactions between PA6 and metals [61,62]. AA6061 is an alloy containing various compositional elements and is always prone to have oxide and hydroxide layers when exposed to atmospheric conditions. In addition, hydrocarbon contaminations are

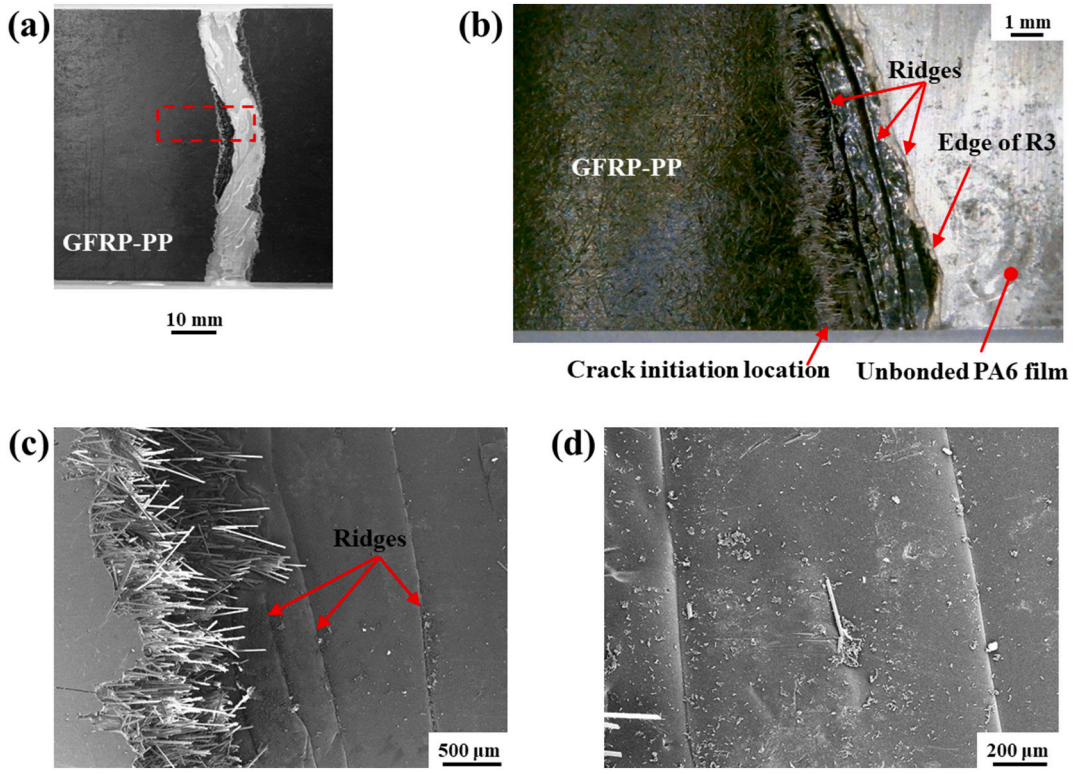

Fig. 11. Resolidified PA6 near fracture origin in the joint [1800 rpm, 0.10 mm and 12 s], (a) global view, (b) local view of PA6 + PP reconsolidation near through crack fracture region, (c) SEM micrograph of crack front location and ridges, (d) ridges pattern on the aluminum side.

likely to be present before and during the welding process, suggesting various combinations of chemical interactions between aluminum surface and PA6. On the other end, both PA6 and PP matrices are found to have a strong network via the glass fibers and form a strong interface at the AA6061. The boundaries of AA6061 and PA6 are indistinguishable in Fig. 7(c), suggesting a strong and intimate bonding between both materials at the molecular level. Further quantification of chemical and physical bonding types at an atomic or molecular level is out of the scope of this study.

Another important feature of bonded regions observed in Fig. 5 is further illustrated in detail in Fig. 10. All these bonded regions are predominantly circular and are found to be playing a significant role in joint quality. The placement of the friction tool and the distances from all the joint boundaries were maintained to keep the joint geometry symmetric with respect to the tool center and tool surface area. Edges of the joint were maintained square of 70 mm × 70 mm and a minimum one-tool diameter distance was maintained between the tool edge and the joint's outer edges providing a significant space to contain the pressure generated during the tool plunging and polymer melting during the joining process. Additionally, the spread of the melting zone increases more compared to the concentration of the decomposition zone around the tool impression (Figs. 5 a–j and 9d) which signifies a fully developed joint under the 12-s spot weld condition for the said material combination. This can potentially happen when the interfacial contact regions have reached the melting point of both the PA6 and the PP matrix material, as can be seen from the corresponding temperature profiles in Fig. 9(c) for an approximately stable thermal regime beyond 6-s spot weld time. Further analysis to understand the effect of pressure containment and optimization corresponding to the tool and joint sizing and tool placement will be considered in future studies.

Based on the macro and microscopic observations discussed above, the bond formation process can be described as illustrated in Fig. 12, starting from polymer melting, to melt flow and melt re-solidification, leading to a multi-material composite network at the joint interface (see Fig. 12a–b). As seen in the previous sections, spot weld time plays a vital role in forming a strong joint. With a sufficient spot weld time, e.g., 12 s (see Section 3.2), the general characteristics of the bonded region and its development process follow as those shown in Fig. 12(a) and (b). As such, cavity-rich volume in R1, wide spread of PA6 forming a composite with glass fibers of GFRP-PP in R2, and evolution of ridges in R3 are shown in Fig. 12(a). Fully developed bonding regions on aluminum and GFRP-PP sides along with ridges in R3 are shown in Fig. 12(b).

4.2. Process characteristics

The proposed friction spot joining process for achieving metal-polymer joining has only four process parameters to control (tool dimension, rpm, forge depth, and spot weld time). It can be directly extended for performing friction lap seam welding which can be used to achieve metal-polymer continuous joints and has numerous advantages [11,13]. The process offers several major advantages over existing joining processes, including (i) direct control of the bonded region through friction heating tool dimension, (ii) high welding speed without requiring special surface or bulk material treatments, (iii) energy-saving and environmentally friendliness due to the absence of filler or masking gas, voltage sparks, and minimal material loss during friction heat generation. In addition, the application of an inexpensive and readily available PA6 thin film interlayer makes the process highly cost-effective. Note that PA6 thin film cost only around 1.50 cents per square inch of the joint produced between AA6061 and GFRP-PP in the laboratory which is significantly lower than other surface and material modification methods necessary to join said materials for load-bearing structural applications. After achieving the high quality joining under the current sample and material conditions, another future study of process parameter optimization is underway and is expected to bring forth an optimally short processing time aptly suited for automotive applications through the acquisition of a dedicated machine and control system.

5. Conclusions

A simple and reliable process for joining nonpolar polymer composite to metal is presented and has been successfully demonstrated for joining AA6061 and GFRP-PP in a spot weld configuration by seeding functional groups through a readily available PA6 thin film as an interlayer. The major conclusions of the presented work can be summarized as follows.

1. Reliable joining between AA6061 and GFRP-PP, which traditionally cannot be accomplished without special surface or material

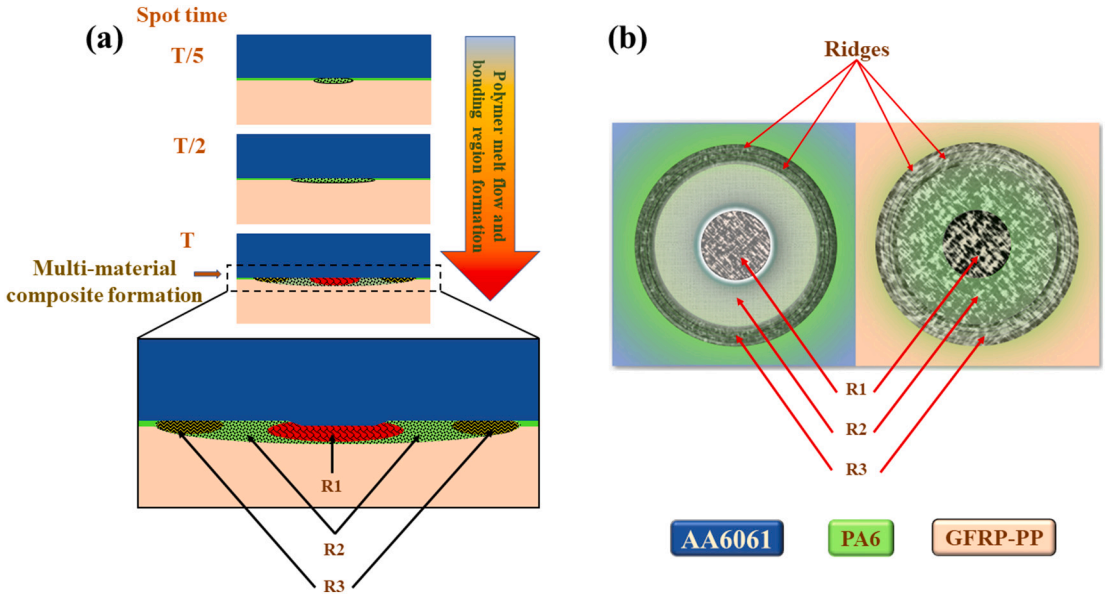

Fig. 12. (a) Schematic representation of multi-material composite network formation at the cross-section of AA6061/GFRP-PP joint (T = 12 s), (b) schematic representation of the fully developed bonding regions for a 12-s spot-welded joint.

modifications, can now be achieved through a simple functional group seeding technique using a PA6 thin film. The joint failure load increases from zero (no joining condition), without the PA6 film insert, to 11.52 kN (BM failure) when using the PA6 film insert. The new process proves to be simple and cost-effective, particularly in a high-volume production environment.

2. Although this study was not intended to develop a detailed process parameter window for a specific application, the experimental results show that the proposed joining process possesses just a few parameters to control for ensuring bond quality consistency. Chief among them are weld time (12 s for the material combination used) which governs the final interfacial bonding area, and preset forge depth (corresponding to the 150 N preset force) which ensures initial intimate contact at the joint interface. As a result, the process can be readily adapted to various applications for joining nonpolar polymeric composites to metals.
3. The application of PA6 provided the necessary interfacial bridging between the non-joinable AA6061 and the GFRP-PP. The interfacial bonding mechanisms observed can be attributed to (1) direct bonding between aluminum and PA6 (resulting from PA6 film) through previously proven C-O-Al type chemical bonding and; (2) the formation of a strong multi-material composite network of PA6, glass fibers, and PP matrix, leading to a strong AA6061/GFRP PP joint.

CRediT authorship contribution statement

A.S. Khan: Conceptualization, Methodology, Validation, Investigation, Writing – original draft, Writing – review & editing. **F. Liu:** Conceptualization, Resources, Writing – review & editing, Supervision. **P. Dong:** Conceptualization, Methodology, Resources, Writing – review & editing, Supervision, Funding acquisition.

Declaration of competing interest

The authors declare the following financial interests/personal relationships which may be considered as potential competing interests:

Abdul Sayeed Khan, Pingsha Dong, and Fengchao Liu have filed a patent application (U.S. Provisional Application No. 63/391,030).

Data availability

The datasets generated and/or analyzed in the current study are available from the corresponding author on reasonable request.

Acknowledgements

This work was supported in part by the University of Michigan College of Engineering research incentive grant and a grant from the National Science Foundation (NSF CMMI 2126163).

References

[1] Sperling D, Cannon JS. Reducing climate impacts in the transportation sector. Springer; 2009.
[2] Taub A, De Moor E, Luo A, Matlock DK, Speer JG, Vaidya U. Materials for automotive lightweighting. Annu Rev Mater Res 2019;49:327–59. https://doi.org/10.1146/annurev-matsci-070218-010134.
[3] Dong P. Quantitative weld quality acceptance criteria: an enabler for structural lightweighting and additive manufacturing. Weld J 2020:99.
[4] Liu F, Dong P. Directly and Reliably Welding Plastic to Metal. Weld J 2022;101:45–8.
[5] Peter WH, Love LJ, Chesser PC, Gaul KT. Hybrid multi-material endoskeleton overmolded structure for automotive powertrain. Oak Ridge, TN (United States): Oak Ridge National Lab. (ORNL); 2018.
[6] Blanco D, Rubio EM, Marín MM, Davim JP. Advanced materials and multi-materials applied in aeronautical and automotive fields: a systematic review approach. Procedia CIRP 2021;99:196–201. https://doi.org/10.1016/j.procir.2021.03.027.
[7] Pramanik A, Basak AK, Dong Y, Sarker PK, Uddin MS, Littlefair G, et al. Joining of carbon fibre reinforced polymer (CFRP) composites and aluminium alloys – a review. Compos Part A Appl Sci Manuf 2017;101:1–29. https://doi.org/10.1016/j.compositesa.2017.06.007.
[8] Amancio-Filho ST, dos Santos JF. Joining of polymers and polymer–metal hybrid structures: recent developments and trends. Polym Eng Sci 2009;49:1461–76. https://doi.org/10.1002/pen.21424.
[9] Blaga L, Bancilă R, dos Santos JF, Amancio-Filho ST. Friction riveting of glass–fibre-reinforced polyetherimide composite and titanium grade 2 hybrid joints. Mater Des 2013;50:825–9. https://doi.org/10.1016/j.matdes.2013.03.061.
[10] Lambiase F, Scipioni SI, Lee C-J, Ko D-C, Liu F. A state-of-the-art review on advanced joining processes for metal-composite and metal-polymer hybrid structures. Materials (Basel) 2021;14:1890.
[11] Lambiase F, Balle F, Blaga L-A, Liu F, Amancio-Filho ST. Friction-based processes for hybrid multi-material joining. Compos Struct 2021;266:113828. https://doi.org/10.1016/j.compstruct.2021.113828.
[12] Liu, F. and Dong, P., University of Michigan, 2022. *High-speed polymer-to-metal direct joining system and method.* U.S. Patent 11,396,139.
[13] Liu FC, Liao J, Nakata K. Joining of metal to plastic using friction lap welding. Mater Des 2014;54:236–44. https://doi.org/10.1016/j.matdes.2013.08.056.
[14] Liu FC, Dong P, Pei X. A high-speed metal-to-polymer direct joining technique and underlying bonding mechanisms. J Mater Process Technol 2020;280:116610. https://doi.org/10.1016/j.jmatprotec.2020.116610.
[15] Liu FC, Nakata K, Liao J, Hirota S, Fukui H. Reducing bubbles in friction lap welded joint of magnesium alloy and polyamide. Sci Technol Weld Join 2014;19:578–87. https://doi.org/10.1179/1362171814Y.0000000228.
[16] Liu FC, Liao J, Gao Y, Nakata K. Effect of plasma electrolytic oxidation coating on joining metal to plastic. Sci Technol Weld Join 2015;20:291–6. https://doi.org/10.1179/1362171815Y.0000000012.
[17] Wang B, Sun Z, Xu L, Zhang W, Li X, Zhang H. Friction spot joining of aluminum AA5052 and short glass fiber-reinforced PPS: effects of material properties and process parameters on joint structure and strength. J Manuf Process 2021;66:549–64. https://doi.org/10.1016/J.JMAPRO.2021.04.047.
[18] Balle F, Wagner G, Eifler D. Ultrasonic metal welding of aluminium sheets to carbon fibre reinforced thermoplastic composites. Adv Eng Mater 2009;11:35–9.
[19] Feistauer EE, Guimarães RPM, Ebel T, dos Santos JF, Amancio-Filho ST. Ultrasonic joining: a novel direct-assembly technique for metal-composite hybrid structures. Mater Lett 2016;170:1–4. https://doi.org/10.1016/j.matlet.2016.01.137.
[20] Katayama S, Kawahito Y. Laser direct joining of metal and plastic. Scr Mater 2008;59:1247–50.
[21] Wahba M, Kawahito Y, Katayama S. Laser direct joining of AZ91D thixomolded mg alloy and amorphous polyethylene terephthalate. J Mater Process Technol 2011;211:1166–74. https://doi.org/10.1016/j.jmatprotec.2011.01.021.
[22] Huang Y, Gao X, Zhang Y, Ma B. Laser joining technology of polymer-metal hybrid structures - a review. J Manuf Process 2022;79:934–61. https://doi.org/10.1016/J.JMAPRO.2022.05.026.
[23] Tao W, Su X, Chen Y, Tian Z. Joint formation and fracture characteristics of laser welded CFRP/TC4 joints. J Manuf Process 2019;45:1–8. https://doi.org/10.1016/J.JMAPRO.2019.05.028.
[24] Mitschang P, Velthuis R, Didi M. Induction spot welding of Metal/CFRPC hybrid joints. Adv Eng Mater 2013;15:804–13. https://doi.org/10.1002/adem.201200273.
[25] Nagatsuka K, Xiao B, Wu L, Nakata K, Saeki S, Kitamoto Y, et al. Resistance spot welding of metal/carbon-fibre-reinforced plastics and applying silane coupling treatment. Sci Technol Weld Join 2018;23:181–6.
[26] Nagatsuka K, Kitagawa D, Yamaoka H, Nakata K. Friction lap joining of thermoplastic materials to carbon steel. ISIJ Int 2016;56:1226–31. https://doi.org/10.2355/isijinternational.ISIJINT-2016-042.
[27] Liu FC, Dong P, Lu W, Sun K. On formation of AlOC bonds at aluminum/polyamide joint interface. Appl Surf Sci 2019;466:202–9. https://doi.org/10.1016/j.apsusc.2018.10.024.
[28] Han SC, Wu LH, Jiang CY, Li N, Jia CL, Xue P, et al. Achieving a strong polypropylene/aluminum alloy friction spot joint via a surface laser processing pretreatment. J Mater Sci Technol 2020;50:103–14. https://doi.org/10.1016/j.jmst.2020.02.035.
[29] Hussein FI, Akman E, Genc Oztoprak B, Gunes M, Gundogdu O, Kacar E, et al. Evaluation of PMMA joining to stainless steel 304 using pulsed nd:YAG laser. Opt Laser Technol 2013;49:143–52. https://doi.org/10.1016/j.optlastec.2012.12.028.
[30] Meiabadi MSSM, Kazerooni A, Moradi M, Torkamany MJ. Laser assisted joining of St12 to polycarbonate: experimental study and numerical simulation. Optik (Stuttg) 2020;208:164151.
[31] Yusof F, Miyashita Y, Seo N, Mutoh Y, Moshwan R. Utilising friction spot joining for dissimilar joint between aluminium alloy (A5052) and polyethylene terephthalate. Sci Technol Weld Join 2012;17:544–9. https://doi.org/10.1179/136217112x13408696326530.
[32] Al-Sayyad A, Salah F, Bardon J, Hirchenhahn P, Shihata L, Houssiau L, et al. Laser ablation of titanium alloy (Ti64): effects of process parameters on performance of laser welded Ti64–polyamide 6.6 joints. 2021.
[33] Izadi O, Mosaddegh P, Silani M, Dinari M. An experimental study on mechanical properties of a novel hybrid metal–polymer joining technology based on a reaction between isocyanate and hydroxyl groups. J Manuf Process 2017;30:217–25. https://doi.org/10.1016/J.JMAPRO.2017.09.022.
[34] Alaluss K, Bürkner G. Thermal joining of steel/polymer/steel composite materials using non-direct arcprocess technique. J Manuf Process 2018;34:523–30. https://doi.org/10.1016/J.JMAPRO.2018.06.032.

[35] Lambiase F, Grossi V, Paoletti A. Defects formation during friction assisted joining of metals and semi crystalline polymers. J Manuf Process 2021;62:833–44. https://doi.org/10.1016/J.JMAPRO.2020.12.063.
[36] Wang Z, Bi X, Liu B, Xu M, Dong Z. Adhesion enhancement of PEEK/6161-T6 FLJ joints via laser surface modification. Compos Part B Eng 2021;216:108797.
[37] Lambiase F, Paoletti A. Mechanical behavior of AA5053/polyetheretherketone (PEEK) made by friction assisted joining. Compos Struct 2018;189:70–8.
[38] Li Y, Bu H, Yang H, Liu G, Yao J, Zhan X. Effect of laser heat input on the interface morphology during laser joining of CFRTP and 6061 aluminum alloy. J Manuf Process 2020;50:366–79. https://doi.org/10.1016/J.JMAPRO.2019.12.023.
[39] Bu H, Zhan X, Yang H, Wang F, Ma W. Numerical simulation of thermal distribution and residual stress characteristic for laser wobble joining of CFRTP and ti-6Al-4V alloy. J Manuf Process 2022;79:562–75. https://doi.org/10.1016/J.JMAPRO.2022.05.018.
[40] Xie Y, Zhang J, Zhou T. Large-area mechanical interlocking via nanopores: ultra-high-strength direct bonding of polymer and metal materials. Appl Surf Sci 2019;492:558–70.
[41] Ku JH, Jung IH, Rhee KY, Park SJ. Atmospheric pressure plasma treatment of polypropylene to improve the bonding strength of polypropylene/aluminum composites. Compos Part B Eng 2013;45:1282–7. https://doi.org/10.1016/j.compositesb.2012.06.016.
[42] Chen J, Du K, Chen X, Li Y, Huang J, Wu Y, et al. Influence of surface microstructure on bonding strength of modified polypropylene/aluminum alloy direct adhesion. Appl Surf Sci 2019;489:392–402.
[43] Ochoa-Putman C, Vaidya UK. Mechanisms of interfacial adhesion in metal–polymer composites – effect of chemical treatment. Compos Part A Appl Sci Manuf 2011;42:906–15. https://doi.org/10.1016/j.compositesa.2011.03.019.
[44] Liang C-S, Lv Z-F, Bo Y, Cui J-Y, Xu S-A. Effect of modified polypropylene on the interfacial bonding of polymer–aluminum laminated films. Mater Des 2015;81:141–8. https://doi.org/10.1016/j.matdes.2015.05.021.
[45] Astigarraga V, Gondra K, Valea Á, Pardo Aurrekoetxea G. Improvement of adhesive bonding of polypropylene and maleic anhydride grafted polypropylene blends to aluminium by means of addition of cyclic butylene terephthalate. J Adhes 2019;95:286–307. https://doi.org/10.1080/00218464.2018.1437415.
[46] Liu L, Wang Z, Yu Y, Fu S, Nie Y, Wang H, et al. Engineering interfaces toward high-performance Polypropylene/Coir fiber biocomposites with enhanced friction and Wear behavior. ACS Sustain Chem Eng 2019;7:18453–62. https://doi.org/10.1021/acssuschemeng.9b04381.
[47] Kore S, Spencer R, Ghossein H, Slaven L, Knight D, Unser J, et al. Performance of hybridized bamboo-carbon fiber reinforced polypropylene composites processed using wet laid technique. Compos Part C Open Access 2021;6:100185. https://doi.org/10.1016/J.JCOMC.2021.100185.
[48] Alwekar S, Yeole P, Kumar V, Hassen AA, Kunc V, Vaidya UK. Melt extruded versus extrusion compression molded glass-polypropylene long fiber thermoplastic composites. Compos Part A Appl Sci Manuf 2021;144:106349. https://doi.org/10.1016/j.compositesa.2021.106349.
[49] Kleinbaum S, Jiang C, Logan S. Enabling sustainable transportation through joining of dissimilar lightweight materials. MRS Bull 2019;44:608–12. https://doi.org/10.1557/mrs.2019.178.
[50] Link T, Behnisch F, Rosenberg P, Seuffert J, Dörr D, Hohberg M, et al. Hybrid composites for automotive applications-development and manufacture of a system-integrated lightweight floor structure in multi-material design. In: Proc. SPE 19th annu. automot. compos. conf. exhib. ACCE; 2019.
[51] Chen M-A, Li H-Z, Zhang X-M. Improvement of shear strength of aluminium-polypropylene lap joints by grafting maleic anhydride onto polypropylene. Int J Adhes Adhes 2007;27:175–87. https://doi.org/10.1016/j.ijadhadh.2006.01.008.
[52] Zhu XB, Yang X, Li YB, Carlson BE. Reinforcing cross-tension strength of adhesively bonded joints using metallic solder balls. Int J Adhes Adhes 2016;68:263–72. https://doi.org/10.1016/J.IJADHADH.2016.04.009.
[53] Wu T, Zhang Q, Zhang C, Li YB, Carlson BE. Process variables influencing solder reinforced adhesive (SRA) performance. J Manuf Process 2018;31:440–52. https://doi.org/10.1016/J.JMAPRO.2017.12.001.
[54] Kang HT, Dong P, Hong JK. Fatigue analysis of spot welds using a mesh-insensitive structural stress approach. Int J Fatigue 2007;29:1546–53. https://doi.org/10.1016/J.IJFATIGUE.2006.10.025.
[55] Lu H, Dong P, Boppudi S. Strength analysis of fillet welds under longitudinal and transverse shear conditions. Mar Struct 2015;43:87–106. https://doi.org/10.1016/J.MARSTRUC.2015.06.003.
[56] Zhang Y, Dong P, Pei X. Fracture mechanics modeling of fatigue behaviors of adhesive-bonded aluminum alloy components. Metals (Basel) 2022:12. https://doi.org/10.3390/met12081298.
[57] La Mantia FP. Blends of polypropylene and nylon 6: influence of the compatibilizer, molecular weight, and processing conditions. Adv Polym Technol J Polym Process Inst 1993;12:47–59.
[58] Rahman NA, Hassan A, Yahya R, Lafia-Araga RA. Glass fiber and nanoclay reinforced polypropylene composites:morphological, thermal and mechanical properties. 2013.
[59] Sang L, Wang C, Wang Y, Wei Z. Thermo-oxidative ageing effect on mechanical properties and morphology of short fibre reinforced polyamide composites – comparison of carbon and glass fibres. RSC Adv 2017;7:43334–44. https://doi.org/10.1039/C7RA07884F.
[60] Goushegir SM, dos Santos JF, Amancio-Filho ST. Friction spot joining of aluminum AA2024/carbon-fiber reinforced poly(phenylene sulfide) composite single lap joints: microstructure and mechanical performance. Mater Des 2014;54:196–206. https://doi.org/10.1016/j.matdes.2013.08.034.
[61] Zhao S, Kimura F, Wang S, Kajihara Y. Chemical interaction at the interface of metal–plastic direct joints fabricated via injection molded direct joining. Appl Surf Sci 2021;540:148339.
[62] Hirchenhahn P, Al Sayyad A, Bardon J, Felten A, Plapper P, Houssiau L. Highlighting chemical bonding between nylon-6.6 and the native oxide from an aluminum sheet assembled by laser welding. ACS Appl Polym Mater 2020;2:2517–27.